



## Hydrologic and atmospheric controls on initiation of convective precipitation events

Jehn-Yih Juang,<sup>1</sup> Amilcare Porporato,<sup>1,2</sup> Paul C. Stoy,<sup>1</sup> Mario S. Siqueira,<sup>1</sup>  
A. Christopher Oishi,<sup>1</sup> Matteo Detto,<sup>3</sup> Hyun-Seok Kim,<sup>1</sup> and Gabriel G. Katul<sup>1,2</sup>

Received 7 February 2006; revised 21 July 2006; accepted 30 October 2006; published 16 March 2007.

[1] The pathway to summertime convective precipitation remains a vexing research problem because of the nonlinear feedback between soil moisture content and the atmosphere. Understanding this feedback is important to the southeastern U. S. region, given the high productivity of the timberland area and the role of summertime convective precipitation in maintaining this productivity. Here we explore triggers of convective precipitation for a wide range of soil moisture states and air relative humidity in a mosaic landscape primarily dominated by hardwood forests, pine plantations, and abandoned old field grassland. Using half-hourly sensible heat flux, micrometeorological, hydrological time series measurements collected at adjacent HW, PP, and OF ecosystems, and a simplified mixed layer slab model, we developed a conditional sampling scheme to separate convective from nonconvective precipitation events in the observed precipitation time series. The series analyzed (2001–2004) includes some of the wettest and driest periods within the past 57 years. We found that convective precipitation events have significantly larger intensities (mean of 2.1 mm per 30 min) when compared to their nonconvective counterparts (mean of 1.1 mm per 30 min). Interestingly, the statistics of convective precipitation events, including total precipitation, mean intensity, and maximum intensity, are statistically different when convective precipitation is triggered by moist and dry soil conditions but are robust in duration. Using the data, we also showed that a “boundary line” emerges such that for a given soil moisture state, air relative humidity must exceed a defined minimum threshold before convective precipitation is realized.

**Citation:** Juang, J.-Y., A. Porporato, P. C. Stoy, M. S. Siqueira, A. C. Oishi, M. Detto, H.-S. Kim, and G. G. Katul (2007), Hydrologic and atmospheric controls on initiation of convective precipitation events, *Water Resour. Res.*, 43, W03421, doi:10.1029/2006WR004954.

### 1. Introduction

[2] The southeastern United States (SE) timberland ecosystems are among the most productive in North America and act as an important carbon sink within the continental United States [Houghton *et al.*, 1998; Schimel, 1995; Tans and White, 1998]. (In this study, the SE includes the states of Alabama, Arkansas, Florida, Georgia, Louisiana, Mississippi, North Carolina, South Carolina, Tennessee, Virginia, and the eastern part of Oklahoma and Texas. This definition is consistent with that of Findell and Eltahir [2003a, 2003b]. However, this region is classified as the “Southern Region” by U.S. Department of Agriculture (USDA) [Wear and Greis, 2002].) This high productivity is attributable to the moderate climate (mean annual temperature  $\sim 15.5^\circ\text{C}$ ) and to the ample precipitation during

the growing season ( $\sim 95 \text{ mm month}^{-1}$  from April to September). In a recent land use assessment, the USDA estimated that the timberland cover of the SE ecosystems over the past half century (since 1953) experienced minor fluctuations ( $\sim \pm 3.1\%$  with a minimum of 793 thousand  $\text{km}^2$  in 1989 and a maximum of 845 thousand  $\text{km}^2$  in 1956), and currently represents  $\sim 48\%$  of the SE land cover area [Wear and Greis, 2002]. However, the composition of the timberland cover is undergoing significant changes. For example, planted pine ecosystems comprised  $\sim 30\%$  of the combined pine plantation and upland hardwood forest area in 1995, a ratio expected to increase to 50% in 2040 [Wear and Greis, 2002]. The precipitation mechanism likely to be impacted by such land cover change is convective precipitation because of its sensitivity to the local land-atmosphere heat and moisture exchange rates. To date, the implications of such projected land cover change on precipitation patterns in this region remain a vexing problem because of the numerous nonlinear feedback mechanisms between soil moisture content and the atmospheric state, though several model results and field experiments are beginning to offer preliminary clues [Atlas *et al.*, 1993; D’Odorico and Porporato, 2004; Findell and Eltahir, 2003b; Giorgi *et al.*, 1996; Pan *et al.*, 1996; Trenberth and Guillemont, 1996].

<sup>1</sup>Nicholas School of the Environment and Earth Sciences, Duke University, Durham, North Carolina, USA.

<sup>2</sup>Department of Civil and Environmental Engineering, Duke University, Durham, North Carolina, USA.

<sup>3</sup>Dipartimento di Ingegneria Idraulica, Ambientale, Infrastrutture viarie e del Rilevamento, Politecnico di Milano, Milan, Italy.

[3] Using model simulations based on coupling the convective triggering potential index (CTP) with the low level humidity index ( $HI_{low}$ ), *Findell and Eltahir* [2003a, 2003b] concluded that the feedback between soil moisture and subsequent convective precipitation in the SE region is positive, meaning that subsequent convective precipitation events are highly correlated to wet soil moisture states in the early morning hours and to high evapotranspiration during the morning and early afternoon.

[4] Field experiments at a shallow-rooted SE planted loblolly pine forest suggest that pine ecosystems can be highly sensitive to episodic short-term droughts [*Oren et al.*, 1998]; long-term sap flow measurements in a loblolly pine plantation showed that a decrease in volumetric soil moisture content within the root zone ( $\theta$ ) from 0.20 to 0.14 reduces their transpiration rate ( $T_r$ ) by a factor of 3 [*Oren et al.*, 1998]. When this sensitivity of  $T_r$  to  $\theta$  is placed within the context of the projected increase in pine plantation area, the positive feedback alluded to by *Findell and Eltahir* [2003a, 2003b] may be significantly disrupted by episodic droughts.

[5] A starting point to explore such interactions between soil and atmospheric water states is to investigate the interplay between the triggers of convective precipitation and environmental factors in a region whose  $T_r$  is known to be sensitive to  $\theta$ . To characterize how this interplay could be altered by the land use change, we conduct this investigation in a SE landscape that is composed of different land cover types yet experiences the same climatic, hydrologic, and edaphic conditions. The minimal environmental factors to be analyzed must involve  $\theta$ , ambient atmospheric relative humidity ( $RH$ ), and the physiological controls on land surface energy budget (i.e., sensible/latent heat fluxes). We investigate this interplay by combining a long-term half-hourly precipitation record, measured sensible heat flux from eddy covariance monitoring systems in this mosaic, ambient mean air temperature and relative humidity, and nearby early morning sounding profiles representing the upper atmospheric properties. Even within this restricted scope, numerous simplifications must be invoked to separate convective precipitation from other precipitation patterns and to track its dependence on antecedent  $\theta$  and  $RH$ .

[6] To accomplish this objective, we limited our analysis to periods spanning late spring to early fall (May to September, Julian day 121 to day 273), which is defined here as “summertime”. This is roughly the period when the leaf area index (LAI) is either at or approaching its maximum value thereby providing some basis to investigate the effects of ecophysiological controls on convective precipitation events [*McCarthy et al.*, 2006].

[7] The analysis was organized as follows: we first developed a simplified model to stratify the long-term measured precipitation record into convective and nonconvective conditions. We then analyzed the statistics of convective precipitation with respect to their nonconvective counterpart to assess their overall contribution to growing season precipitation during the study period. Next, the statistics of convective precipitation for different combination of  $\theta$  and  $RH$  regimes are considered. Particular attention was devoted to whether the statistics of convective precipitation triggered by dry water states (low  $\theta$  and low  $RH$ ) differ from their moist counterparts. We restricted our

research area to a local-scale SE mosaic landscape composed of three different vegetated land cover types, and the analysis was conducted using an effective area-averaged measurements. Hence this analysis did not explicitly consider the heterogeneity or clustering of the vegetation within the landscape, which when it exists at sufficiently large scales (5–50 km), can alter the exchange of water between the surface and atmosphere and influence the onset of the fraction of low cloud cover, area-averaged cloud amount [*Wetzel*, 1990] and the precipitation patterns.

## 2. Experimental Site and Measurements

[8] Much of the site and experimental setup are described elsewhere [*Novick et al.*, 2004; *Palmroth et al.*, 2005; *Stoy et al.*, 2005]; however, the salient points are repeated for completeness.

[9] The data used here were collected at the Blackwood Division of the Duke Forest near Durham in North Carolina (35°58'N, 79°05'W, 163 m above sea level) as part of FluxNet, an ongoing global long-term CO<sub>2</sub> flux monitoring initiative [*Baldocchi et al.*, 2001]. The local topographic variations are small (slope <0.5%) such that the effect of the complex terrain on the micrometeorological measurements can be ignored [*Siqueira et al.*, 2002]. The soil type is acidic Hapludalf with a clayey loam (Enon silt loam) in the upper 0.3 m above a clay layer, which extends to bedrock at ~0.7 m (Soil Survey of Orange County, North Carolina, 1975). The saturated soil moisture content within the rooting zone is 0.54 m<sup>3</sup> m<sup>-3</sup> [*Oren et al.*, 1998]. Using data collected from a nearby weather station (Chapel Hill 2 E, location: 35°55'N/79°05'W, 156.1 m above sea level), the long-term (from 1948 to 2004) mean annual precipitation is 1185 ± 117 mm, and the annual mean air temperature is 14.9 ± 0.9°C.

[10] This site comprises three different major land cover types: an abandoned old field covered with grass and herbaceous species (OF), a 22-year-old (in 2005) maturing loblolly pine (*Pinus taeda*) forest (PP), and an 80 to 100-year-old mature oak-hickory (*Quercus* and *Carya* species) deciduous hardwood forest (HW). These three land cover types represent a typical land use sequence after abandonment of agricultural fields in the piedmont region of North Carolina [*Oosting*, 1942]. The OF and PP sites were established after a clear-cut and burn in 1979 and 1983, respectively. The OF site is mowed regularly every year to prevent the encroachment of woody species. At the PP site, the pine seedlings were planted at 2 m × 2.4 m spacing in 1983. The characteristics of the experimental site and each land cover are summarized in Table 1.

[11] This region experienced a mild drought event in 2001 and a severe drought event in 2002 during the growing season. The 2001 to 2004 growing season precipitation records nearly covered the wettest and driest states within the past 57 years on record (see Figure 1, top), thereby providing a wide range of soil moisture and air relative humidity conditions. Figure 1 (bottom) shows the distributions of  $\theta$  in each land cover from 2001 to 2004, and suggest that higher  $\theta$  values were more frequently observed in the HW site than the other two ecosystems. In Figure 1 (bottom), the solid line shows the ensemble area-weighted (see discussion in section 4) averaged distribution of  $\theta$  from the three land covers, and the vertical line of  $\theta = 0.2$  m<sup>3</sup> m<sup>-3</sup>

**Table 1.** Site Description for Each Ecosystem and a Summary of the Setup at the Blackwood Division of the Duke Forest Near Durham, North Carolina

	Site		
	PP	HW	OF
Land cover type	planted pine	hardwood forest	old-field grassland
Dominant canopy species	<i>Pinus taeda</i> L. with few <i>Liquidambar styraciflua</i> L.	composed of <i>Liriodendron tulipifera</i> L., <i>Quercus alba</i> L., <i>Q. michauxii</i> Nutt., <i>Q. phellos</i> L., <i>L.styraciflua</i> L., and <i>Carya</i> ssp.	$C_3$ grass <i>Festuca arundinaria</i> shrub with few other $C_3$ herbs and $C_4$ grass
Age/management	22 years (since 1983)	80–100 years	mowed once or twice per year (since the clear-cut in 1979)
Canopy height	18.0 m	25.0 m	0.1 to 1.0m
Leaf area index	2.5 – 5.5 $m^3m^{-3}$	0.2 – 7.0 $m^3m^{-3}$	1.0 – 3.0 $m^3m^{-3}$
Tower height	22.2 m	41.8 m	4.8 m
Eddy covariance system height	20.2 m	39.8 m	2.8 m
Soil moisture measurement	24 sensors	12 sensors	6 sensors

approximately represents the mode of this ensemble distribution for the dry soil condition.

[12] Satellite multispectral data (IKONOS satellite, Space Imaging, Thornton, CO, USA) were acquired at 4 m × 4 m spatial resolution to analyze the composition of the land

cover and to characterize the dominant vegetation in the vicinity of the study site. A 10 km × 10 km area (Figure 2) around the study site (red rectangular region in Figure 2) acquired on 23 September 2004 was chosen to determine the dominant land cover likely to impact triggers of con-

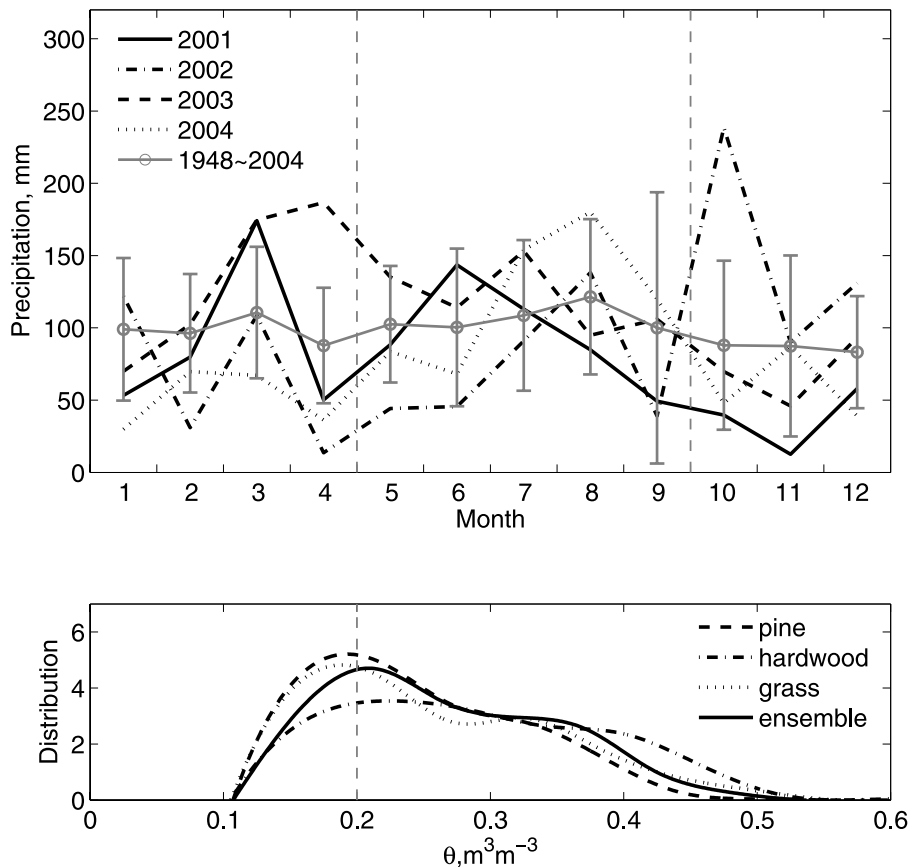


**Figure 1.** (top) Time variation of ensemble-averaged monthly precipitation and (bottom) the probability density function (pdf) of  $\theta$  for each vegetation cover from 2001 to 2004. The area-weighted ensemble soil moisture PDF is also shown for reference.

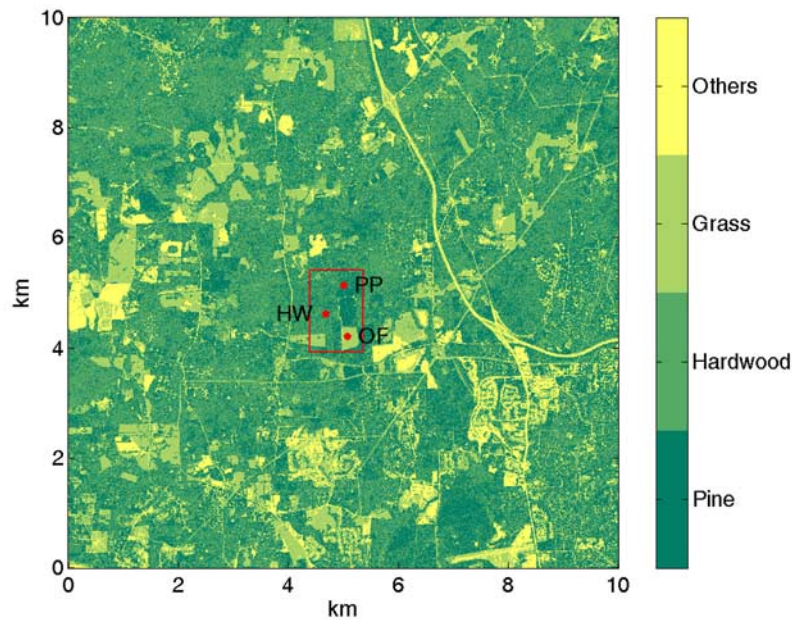


**Figure 2.** Composition of different vegetation cover from the IKONOS image ( $4 \text{ m} \times 4 \text{ m}$  spatial resolution) in the vicinity of the Blackwood Division of Duke Forest (the area within the red rectangular region). The image was acquired on 23 September 2004. The walkup towers with long-term monitoring systems at all three different ecosystems are marked as red dots.

vective precipitation. This area is sufficiently larger than a typical convective cell [Stull, 1988]. Applying the parallelepiped algorithm [Detto *et al.*, 2006; Richards, 1999], the normalized difference vegetation index (NDVI) was computed from surface reflectance averaged over the spectral wavelengths from visible red to near infrared regions, and the surface vegetation cover was then stratified. The color map in Figure 2 shows the spatial distribution of four different land covers in the  $10 \text{ km} \times 10 \text{ km}$  area around the study site. From this analysis, the fraction of pine forest, hardwood forest, grass, and other land cover types (e.g., road and residential areas) are 33.3 %, 41.6 %, 16.8 %, and 8.3%, respectively. This composition is used to derive area-weighted quantities of all the model parameters as described in section 4.

[13] The long-term environmental and land surface flux data were sampled above each ecosystem (see Figure 2). The half-hourly tipping bucket precipitation, mean air temperature, mean air relative humidity, incident shortwave radiation, and eddy covariance measured sensible and latent heat fluxes were all collected above each canopy type. The volumetric soil moisture content within the rooting zone (the top 0.3 m region) was measured around each tower.

[14] In addition to the long-term measurements collected at the Duke Forest, the upper atmospheric characteristics were determined from early morning sounding data sampled at a nearby airport and were used to determine the lapse rate needed to determine the boundary layer dynamics described next.

### 3. Data Analysis

[15] To address the study objective, we developed a methodology to conditionally sample summertime convective precipitation from the long-term precipitation record

measured by a tipping bucket gauge. The conditional sampling scheme utilized a simple slab model to determine the evolution of both the mixed layer height ( $z_i$ ) and the lifting condensation level ( $H_{LCL}$ ). The dynamics of  $z_i$  is mainly driven by the measured surface sensible heat flux, and the value of  $H_{LCL}$  is determined from the measured near-surface air temperature, air humidity, and atmosphere pressure. The convective precipitation events from the long-term record were identified by checking whether modeled  $z_i$  intersects modeled  $H_{LCL}$  just prior to the observed rainfall event (see section 4) thereby marking this event as convective. Next, we briefly describe how  $z_i$ ,  $H_{LCL}$ , and the identification scheme are implemented.

#### 3.1. Mixed Layer Height Evolution

[16] To determine the temporal evolution of the mixed layer height ( $z_i$ ), the entire mixed layer is treated as a single slab that has a mean slab potential temperature  $\overline{T}_p$ , where the overbar represents the temporal averaging operator over turbulent fluctuation (30 min in this study). By ignoring the heat source/sink terms within the slab volume and adopting a standard encroachment assumption [Garc *et al.*, 2002; Stull, 1976, 1988], the integrated one-dimensional continuity equation reduces to

$$\frac{dz_i}{dt} = \frac{\overline{w'T'_{ps}} - \overline{w'T'_{pz_i}}}{\gamma z_i}, \quad (1)$$

where  $\overline{w'T'_{ps}}$  and  $\overline{w'T'_{pz_i}}$  individually represent the turbulent sensible heat fluxes at the surface and at the top of the mixed layer,  $\gamma$  is the local lapse rate of  $\overline{T}_p$  just above  $z_i$ , and the primed quantities denote turbulent excursions around their time-averaged values.

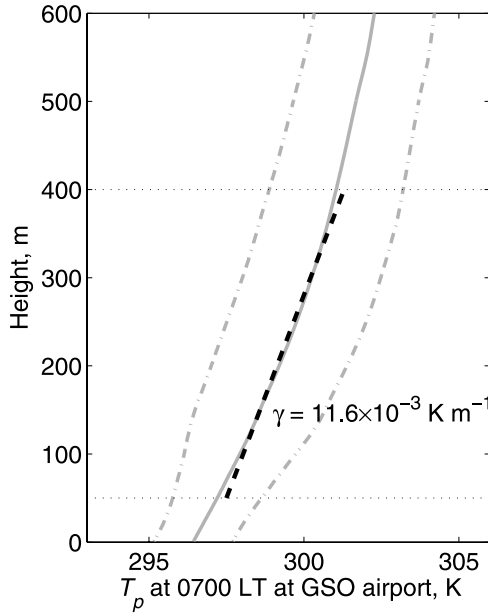


**Figure 3.** Ensemble profiles of potential temperature from 1998 to 2004 collected at the Piedmont Triad International Airport (GSO). The solid line shows the mean value, the dot-dashed lines are one standard deviation from the mean, and the dashed line is the mean lapse rate determined between 50 and 400 m.

[17] As earlier stated, the surface sensible heat flux  $\overline{w'T'_{ps}}$  is directly measured from the eddy covariance system for each land cover and then aggregated using an area-weighted scheme; however, the lapse rate  $\gamma$  and the entrainment flux  $\overline{w'T'_{pz_i}}$  are additional unknowns that require further parameterizations.

### 3.2. Determination of Lapse Rate ( $\gamma$ ) and Entrainment Flux ( $\overline{w'T'_{pz_i}}$ )

[18] We used the daily upper air sounding profiles at Piedmont Triad International Airport (GSO, 36°05'N, 79°57'W, 270 m above sea level and 79 km west of the Duke Forest) to estimate the value of  $\gamma$ . The sounding data are maintained by the Department of Atmospheric Science at University of Wyoming, and is collected at 0000 UT (local time 0700 LT) and 1200 UT (local time 1900 LT) every day. We estimated the early morning lapse rate  $\gamma$  at the top of the mixed layer from the mean value of the potential temperature profile at 0700 LT between the height of 50 m and 400 m from 2001 to 2004. Figure 3 shows the ensemble value of the sounding profiles and the resultant mean  $\gamma = 11.6 \times 10^{-3} \text{ }^\circ\text{C m}^{-1}$ . This estimate is about 18% larger than the dry adiabatic lapse rate, given by  $g/C_p = 9.76 \times 10^{-3} \text{ }^\circ\text{C m}^{-1}$ , where  $g = 9.81 \text{ m s}^{-2}$  is the gravitational acceleration, and  $C_p \sim 1005 \text{ J Kg}^{-1} \text{ }^\circ\text{C}^{-1}$  is the specific heat capacity of dry air at constant pressure.

[19] As for the estimate of the entrainment flux from the top of the mixed layer,  $\overline{w'T'_{pz_i}}$ , we adopt the standard parameterization used in encroachment models:  $\overline{w'T'_{pz_i}} = -\beta \overline{w'T'_{ps}}$  [Tennekes, 1973].

[20] Although the value of  $\beta$  changes with time of day, several numerical studies and measurements suggest that  $\beta$  is constrained between 0.2 and 0.4 [Betts *et al.*, 1992; Kim

and Entekhabi, 1998]. Here we assumed the value of  $\beta$  to be 0.3 taken from Kim and Entekhabi [1998].  $\beta = 0.3$  and  $\gamma = 11.6 \times 10^{-3} \text{ }^\circ\text{C m}^{-1}$ , the dynamics of  $z_i$  can now be predicted only from the time series of measured surface sensible heat flux  $\overline{w'T'_{ps}}$ .

### 3.3. Lifting Condensation Level

[21] The lifting condensation level is determined from

$$H_{LCL} = \frac{RT_a}{M_a g} \log\left(\frac{P_s}{P_{LCL}}\right), \quad (2)$$

where  $R = 8.314 \text{ J mol}^{-1} \text{ }^\circ\text{C}^{-1}$  is the universal gas constant,  $M_a$  is the molecular weight of the air ( $\sim 29 \text{ g mol}^{-1}$ ),  $P_s$  (kPa) is the atmospheric pressure at the surface, and  $P_{LCL}$  (kPa) is the atmospheric pressure at  $H_{LCL}$ . The value of  $P_{LCL}$  can be approximately determined from the hydrostatic assumption, given by

$$P_{LCL} = P_s \left(\frac{T_{LCL}}{T_a}\right)^{3.5}, \quad (3)$$

where  $T_{LCL}$  (K) is the saturation point temperature at  $H_{LCL}$ . The quantity of  $T_{LCL}$  can be derived from the Clausius-Clapeyron equation [Stull, 1988] as

$$T_{LCL} = \frac{2840}{3.5 \ln(T_a) - \ln\left(\frac{P_s r}{0.622 + r}\right) - 7.108} + 55, \quad (4)$$

where  $r$  is the near-surface atmospheric water vapor mixing ratio calculated from the near-surface mean air relative humidity ( $RH$ ), and the parameter 3.5 is given from the inverse of the Poisson constant.

### 3.4. Initial Conditions

[22] Numerical integration of equation (1) commences at sunrise and is terminated at sunset or when the mixed layer height intercepts the lifting condensation level (i.e.,  $H_{LCL} = z_i$ ). The sunrise (when  $t = t_0$ ) and sunset are determined from the solar zenith angle, which vary with time of day and location.

[23] The initial mixed layer height  $z_i(t_0)$  must also be specified each day. To derive this initial value, nighttime-averaged friction velocity  $\langle \overline{u_*} \rangle$ , and the nighttime-averaged surface sensible heat flux  $\langle \overline{w'T'_{ps}} \rangle$  are employed in the equilibrium model by Zilitinkevich [1972]:

$$z_i(t_0) = 0.4 \left( \frac{\langle \overline{u_*} \rangle}{f} \langle |L| \rangle \right)^{1/2}, \quad (5)$$

where the angle brackets represent the mean quantity averaged throughout the nighttime. The parameter 0.4 is a similarity constant [Garratt, 1992],  $f \sim 10^{-4} \text{ s}^{-1}$  is the Coriolis parameter, and  $\langle |L| \rangle$  is the average of the absolute value of the Obukhov length ( $L$ ) derived from  $\langle \overline{u_*} \rangle$  and  $\langle \overline{w'T'_{ps}} \rangle$ :

$$\langle |L| \rangle = \frac{\langle \overline{T_a} \rangle \langle \overline{u_*} \rangle^3}{kg \langle \overline{w'T'_{ps}} \rangle}. \quad (6)$$

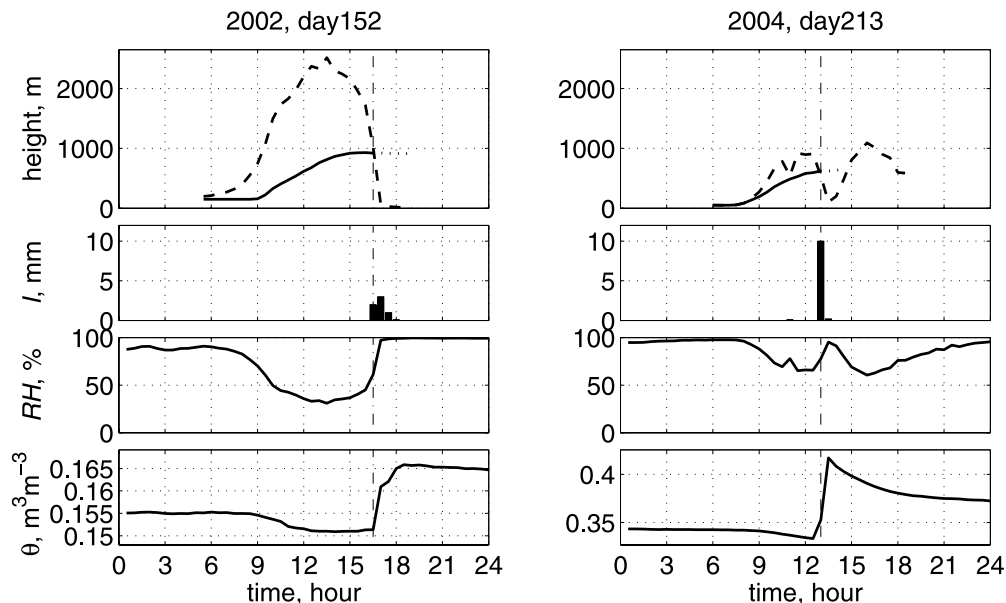


**Figure 4.** Modeled  $z_i$  (solid line) and  $H_{LCL}$  (dashed line) and the corresponding measured precipitation,  $RH$  and  $\theta$ , (left) on day 152 of 2002 and (right) on day 213 of 2004.

[24] Here  $z_i$  is not permitted to drop below 40 m (arbitrarily chosen as double of the PP canopy height). We note that the model simulations are not overly sensitive to the choice of  $z_i(t_0)$  because  $z_i(t_0)$  is often  $<100$  m while the mixed layer height is expected to grow above 1000 m here.

#### 4. Results and Discussions

[25] We used the 2001–2004 summertime (Julian days 121 to 273) record of sensible heat flux, soil moisture content, near surface air temperature, and near surface air relative humidity from each ecosystem to separate convective from nonconvective precipitation. Because the region around the Duke Forest is composed of four major land cover types (pine, hardwood, grassland, and others), yet the slab model is zero-dimensional, a logical starting point is to consider an area-weighted contribution for each of the above variables to soil moisture and sensible heat flux. We ignored the contribution of the class “others” because it is a small fraction of the total area ( $\sim 8.3\%$ ), and rescaled the fractional cover of pine, hardwood and grassland to be 36%, 46%, and 18%, respectively.

##### 4.1. Identification of the Convective Precipitation Events Using the Slab Model

[26] We conditionally sampled the days that are likely to induce convective precipitation events by considering periods that met the following four criteria: (1) The mean incident shortwave radiation  $R_i$  from 1100 LT to 1400 LT was greater than  $600 \text{ W m}^{-2}$ , a surrogate for eliminating days with large midday cloud cover. (2) The area-averaged mean sensible heat flux  $H_s = \rho C_p w' T'_s$  (where  $\rho$  is the air density) from 1100 LT to 1400 LT was greater than  $100 \text{ W m}^{-2}$  to ensure sufficient local heat is produced from the landscape. (3) The atmospheric stability parameter ( $-z/L$ ) was large, namely,  $-z/L \geq 5$ , for  $z = z_i/2$  (i.e., set at the center of the slab volume), and is taken as the stability limit at which free convective turbulence dominates the mixed

layer volume under these conditions. (4) The slab model predicted the occurrence of convective precipitation events when  $z_i = H_{LCL}$  during daytime conditions (i.e., between sunrise and sunset).

[27] To assess the skill of the identification scheme at detecting convective precipitation events, we compared the time at which  $z_i = H_{LCL}$  with the time at which the precipitation event was first detected by the tipping bucket gage. Figures 4 (left) and 4 (right) show an example of the dynamics of  $z_i$ ,  $H_{LCL}$  and the corresponding time series of precipitation,  $RH$  and  $\theta$  for moist (high  $RH$  and  $\theta$ ) and dry (low  $RH$  and  $\theta$ ) conditions, respectively. The effect of soil moisture content on the dynamics of  $z_i$  are evident: dry soil moisture content states induce a relatively deeper mixed layer depth while moist soil moisture states induce shallow convective boundary layers. The comparison shown in Figure 4 also indicates that the model can predict the onset of convective precipitation reasonably well for a wide range of soil moisture states.

[28] To quantify the overall slab model “detection” performance, we compared the predicted and measured convective precipitation timing for all the summertime convective precipitation events from 2001 to 2004 and found that this simple model predicted more than 92 % of the summertime convective precipitation events to occur within 1.5 hour of the observed precipitation timing (Figure 5, recall that the precipitation is measured at 30-min intervals). Note that the pdf of the timing error is skewed toward the negative region. This indicates that the model tends to predict the onset of precipitation slightly earlier (the mean of the pdf curve in Figure 5 is  $-0.18$  hours) than the observed timing. A plausible explanation is that after the mixed layer height intersects the lifting condensation level, a few minutes to few hours may be required to form precipitation in some cases. Naturally, this condition  $z_i = H_{LCL}$  predisposes, but does not necessarily lead to convective precipitation. When air parcels reach  $H_{LCL}$ , condensation forms in regions of negatively buoyant “overshoots of

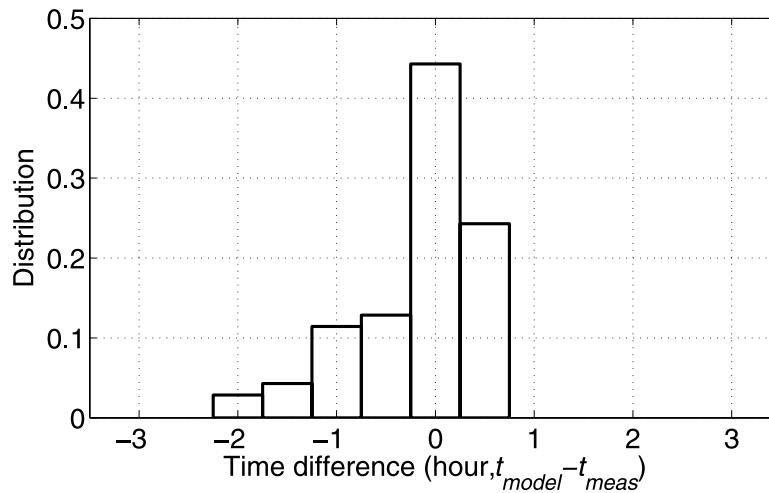


**Figure 5.** Probability density function of the onset time difference between modeled ( $z_i = H_{LCL}$ ) and measured convective precipitation.

mixed layer thermals.” These thermals penetrate the capping inversion at  $z_i$ . If the overshoot is sufficiently strong to continue lifting the condensing air parcel, latent heat is released and its potential temperature becomes sufficiently warmer than its surroundings and it becomes positively buoyant. This height defines the “level of free convection” (LFC). This parcel continues to buoyantly rise until it eventually becomes cooler than its surroundings at which point the “limit of convective” rise (LOC) is attained. Any residual inertia in the parcel might propel it to continue rising further eventually stopping at the cloud top [Emanuel *et al.*, 1994; Stull, 1988]. Once clouds develop, condensation nuclei are required to allow rapid growth of water droplet. When these water droplets reach sufficient size to precipitate and repenetrate the unsaturated air below the cloud base without completely evaporating before reaching the ground surface, rainfall at the surface occurs. Roughly, after  $z_i$  intersects  $H_{LCL}$ , the entire process leading to precipitation detection at the ground may vary from minutes up to 2 hours [Stull, 1988]. This lag between the timing at which  $z_i = H_{LCL}$  and the actual rainfall timing is a plausible explanation of the negative skewness shown in Figure 5. In fact, we did compare the relationship between  $H_{LCL}$  with the LFC under strong convective potential ( $700 \text{ mb} < \text{LFC} < 850 \text{ mb}$ ) estimated from the sounding data at GSO airport for the years 2001 to 2004. The relationship suggests that the difference between LFC at GSO airport and the locally computed  $H_{LCL}$  is not large (difference of  $34 \pm 21 \text{ mbar}$ ). This pressure difference is on the order of 150 m height that is likely to contribute to the skewness reported in Figure 5 assuming that the LFC at GSO airport is identical to the one above the study site.

[29] We also examined the discriminatory skill of the model to distinguish between convective precipitation events ( $z_i$  intercepted by  $H_{LCL}$ ) and nonprecipitation conditions ( $z_i$  did not intersect  $H_{LCL}$ ) when criteria 1–3 were applied (i.e., likely conditions to induce convective precipitation). The slab model correctly detected 86% of the nonprecipitation conditions thereby lending confidence to our approach.

#### 4.2. Statistics of Convective Versus Nonconvective Precipitation

[30] Having identified the convective precipitation events in the precipitation time series, we analyzed their characteristics and contribution to summertime precipitation next. Specifically, we compared the probability density functions (pdf) of the half-hourly intensity for both convective and nonconvective precipitation events (Figure 6).

[31] The comparison shown in Figure 6 suggests that the convective precipitation events have heavier tails than the nonconvective conditions. In fact, the precipitation intensity of the convective precipitation (mean of 2.1 mm per 30 min) is significantly larger than its nonconvective counterpart (mean 1.1 mm per 30 min). We also conducted a Kolmogorov-Smirnov significance test and found that these two pdf distributions in Figure 6 are statistically different at the 99% confidence interval.

#### 4.3. Soil-Atmosphere Water States and Triggers of Summertime Convective Precipitation

[32] Now that properties for summertime convective precipitation events have been identified from the precipitation time series, we explore whether some preferential combination of water states both in the soil and the atmosphere could enhance the triggers of convective precipitation. Using the entire 4-year record, the area-averaged mean soil moisture content  $\theta$  and the measured mean atmospheric relative humidity  $RH$  just prior to each convective precipitation event are shown in Figure 7. For reference, we also show the mean measured  $RH$  and  $\theta$  between 1100 LT and 1500 LT from the entire 4-year record to show that the entire  $RH$ - $\theta$  plane is populated by climatic events. However, the dotted oblique line in Figure 7 represents a clear boundary below which convective precipitation was not observed and likely was not triggered given that the observation record included extremely moist and dry conditions in the region. The reason for the emergence of such “excluded region” is that a relatively dry atmosphere results in very high  $H_{LCL}$  (up to 4000 m) while the relatively moist soil leads to lower sensible heat flux and lower mixed layer heights. Hence this excluded

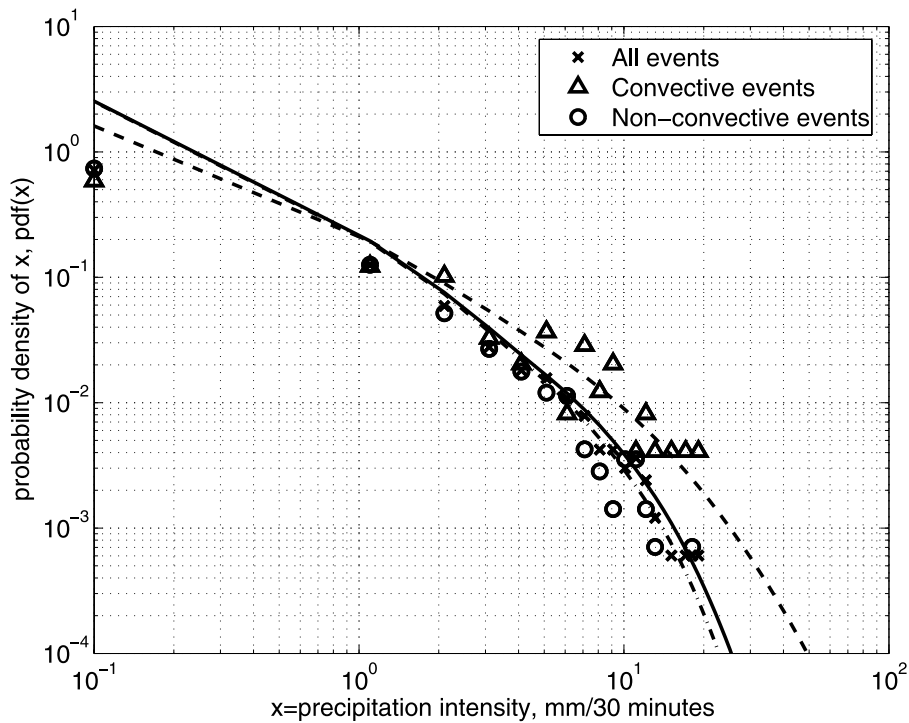


**Figure 6.** Probability density function of convective (triangles and dotted line) and nonconvective (circles and dot-dashed line) precipitation events. The probability density function of all the sampled precipitation events (crosses and solid line) is shown for reference. The solid lines are best fit regression to the data.

region simply reflects the fact that the lifting condensation level in a dry atmosphere cannot intersect the top of the mixed layer for moist soil conditions.

[33] Applying a threshold  $\theta = 0.20 \text{ m}^3 \text{ m}^{-3}$  (dashed lines), the  $RH-\theta$  plane shown in Figure 7 is further decomposed into two regions (moist and dry). The threshold  $\theta = 0.20 \text{ m}^3 \text{ m}^{-3}$  was chosen because it represents the “dry” mode of the ensemble pdf of  $\theta$  shown in Figure 1 (bottom). The bottom left part of Figure 7 (right) shows that conditions with dry soil moisture and dry atmosphere can induce convective precipitation events. An immediate con-

sequence of the existence of precipitation events in the dry soil and dry atmosphere region is that negative feedbacks between soil moisture and subsequent precipitation in the SE region may exist.

[34] To further investigate the characteristics for different soil water states, the pdf of the precipitation duration, maximum half-hourly intensity per event, total precipitation per event, and the mean precipitation intensity were compared separately for soil moisture content above and below  $\theta > 0.20 \text{ m}^3 \text{ m}^{-3}$  (Figure 8). Using the Kolmogorov-Smirnov test, we found that the distributions of precipitation

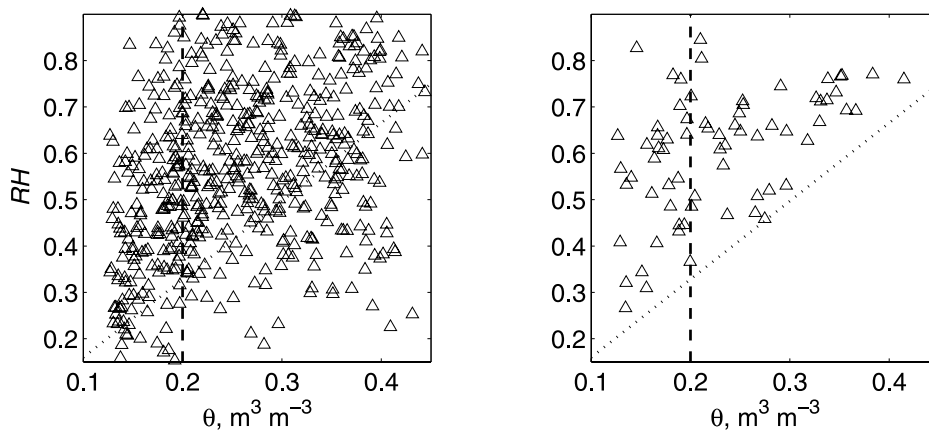


**Figure 7.** (left) Mean measured  $RH$  and  $\theta$  between 1100 and 1500 LT from all data points and (right) the measured  $RH$  and  $\theta$  just before convective precipitation events. The  $\theta = 0.2$  (vertical dashed line) is the mode of the “dry state” in Figure 1, and the dotted line is the boundary below which no precipitation event was observed in the record.

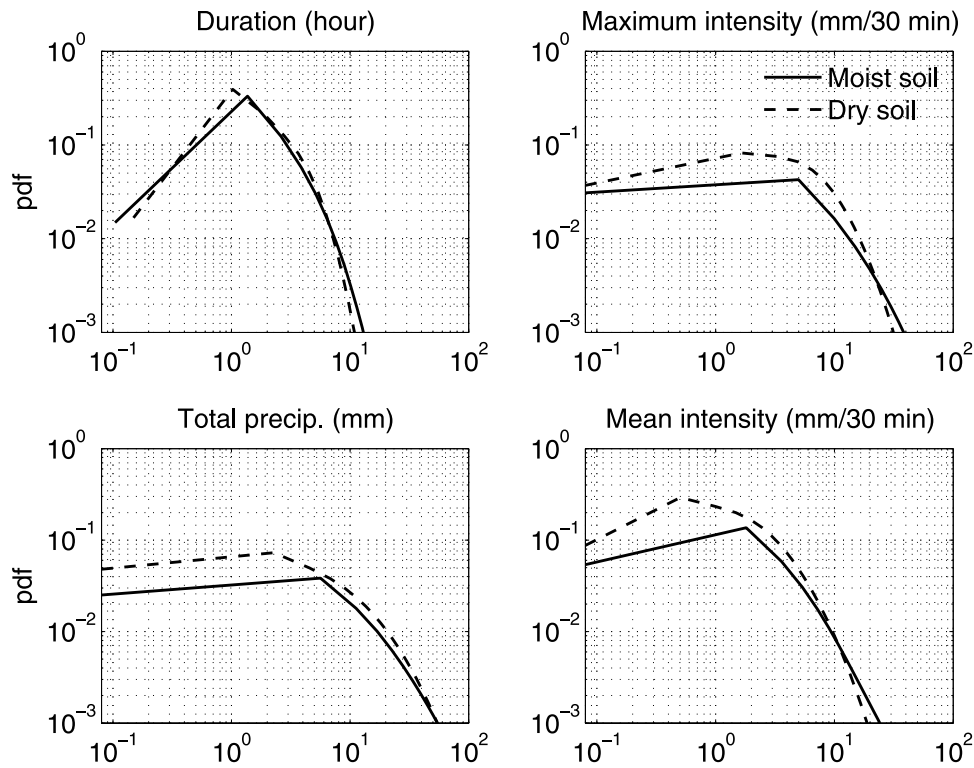


**Figure 8.** Comparison of precipitation statistics for the two soil water states (moist soil and dry soil conditions) shown in Figure 7.

duration of these two soil moisture condition are not significantly different from each other at the 95% confidence interval. However, the distributions of maximum intensity, total precipitation, and the mean intensity are statistically different at the 95% confidence interval. In addition, this statistical comparison also shows that the moist soil condition tends to cause higher maximum intensity, total precipitation, and mean intensity than the dry soil condition in this region.

## 5. Summary and Conclusions

[35] Using a combination of long-term measurements, a simplified mixed layer slab model, and conditional analysis, we demonstrated the following.

[36] 1. The proposed slab model can distinguish between convective and nonconvective precipitation events and is shown to predict the timing of convective precipitation events reasonably well ( $\sim 92.9\%$  within 1.5 hours).

[37] 2. The comparison between the probability density function of the identified convective and nonconvective precipitation events suggests that convective events are significantly more intense (statistically different at the 99% confidence interval).

[38] 3. From the  $RH-\theta$  quadrant analysis, it was shown that the summertime convective precipitation events could be triggered by wet atmosphere and wet soil and by dry atmosphere and dry soil conditions. This suggests that a negative feedback between soil moisture states and convective precipitation may exist in this region.

[39] 4. The statistical comparisons of the precipitation characteristics for these two different soil moisture conditions shows that the moist soil conditions tend to induce

higher maximum intensity and total precipitation than dry soil conditions. However, no statistical difference was detected in the duration.

[40] The proposed approach here takes advantage of the measured sensible heat flux time series to estimate the growth of  $z_i$  and the intersection with  $H_{LCL}$  to “mark” convective precipitation events in point rainfall time series measurements. With the proliferation of FluxNet, a worldwide terrestrial network designed to measure energy and  $CO_2$  fluxes along with climatic and environmental drivers [Baldocchi *et al.*, 2001], it is now possible to extend this methodology to investigate the hydrologic and physiological controls on the pathways to summertime convective precipitation across different climates and biomes. Many sites within FluxNet can now boast in excess of 5 years of measurements, including eddy covariance sensible heat flux, mean air temperature, mean air relative humidity, root zone soil moisture, and point rainfall at half-hourly time-scales. The analysis here may also provide some clues about the interplay between triggers of convective rainfall and actual occurrences of convective rainfall events thereby offering at minimum a probabilistic framework for connecting the land surface trigger to rainfall. For example, using the data set here, we found that during the 2001 to 2004 period, of the 612 growing season days (day 121 to day 273) 162 were “marked” for a convective rainfall trigger and 70 days did register a convective rainfall event. Hence the probability of “realizing” a convective rainfall event knowing that a rainfall trigger did occur is about 45%. What is the relationship between this probability and aerosol loading; how stationary is this probability in light of rapid land use or climatic changes are questions for future

investigations that can be addressed with the availability of long-term data sets originating from FluxNet and land cover data sets.

[41] **Acknowledgments.** This study was supported, in part, by U.S. Department of Energy (DOE) through Terrestrial Carbon Processes (TCP) of the Office of Biological and Environmental Research (BER) and the National Institute of Global Environmental Change (NIGEC) Southeastern Regional Center (SERC) at the University of Alabama (cooperative agreement DE-FC02-03ER63613) and by the National Science Foundation (NSF-EAR and NSF-DMS).

## References

- Atlas, R., N. Wolfson, and J. Terry (1993), The effect of SST and soil moisture anomalies on the GLA model simulations of the 1988 U. S. summer drought, *J. Clim.*, *6*, 2034–2048.
- Baldocchi, D. D., et al. (2001), FLUXNET: A new tool to study the temporal and spatial variability of ecosystem-scale carbon dioxide, water vapor and energy flux densities, *Bull. Am. Meteorol. Soc.*, *82*, 2415–2435.
- Betts, A. K., R. L. Desjardins, and J. MacPherson (1992), Budget analysis of the boundary layer grid flights during FIFE 1987, *J. Geophys. Res.*, *97*, 18,533–18,546.
- Detto, M., N. Montaldo, J. D. Albertson, M. Mancini, and G. Katul (2006), Soil moisture and vegetation controls on evapotranspiration in a heterogeneous Mediterranean ecosystem on Sardinia, Italy, *Water Resour. Res.*, *42*, W08419, doi:10.1029/2005WR004693.
- D’Oroico, P., and A. Porporato (2004), Preferential states in soil moisture and climate dynamics, *Proc. Natl. Acad. Sci. U. S. A.*, *101*, 8848–8851.
- Emanuel, L. A., J. D. Neelin, and C. S. Bretherton (1994), On large-scale circulations in convecting atmospheres, *Q. J. R. Meteorol. Soc.*, *120*, 1111–1143.
- Findell, K. L., and E. A. B. Eltahir (2003a), Atmospheric controls on soil moisture-boundary layer interactions. part I: Framework development, *J. Hydrometeorol.*, *4*, 552–569.
- Findell, K. L., and E. A. B. Eltahir (2003b), Atmospheric controls on soil moisture-boundary layer interactions. Part II: Feedbacks within the continental United States, *J. Hydrometeorol.*, *4*, 570–583.
- Garc, J. A., M. L. Cancillo, and J. L. Cano (2002), A case study of the morning evolution of the convective boundary layer depth, *J. Appl. Meteorol.*, *41*, 1053–1059.
- Garratt, J. R. (1992), *The Atmospheric Boundary Layer*, Cambridge Univ. Press, New York.
- Giorgi, F., L. O. Meams, C. Shields, and L. Mayer (1996), A regional model study of the importance of local versus remote controls of the 1988 drought and 1993 flood over the central United States, *J. Clim.*, *9*, 1150–1162.
- Houghton, R. A., E. A. Davidson, and G. M. Woodwell (1998), Missing sinks, feedbacks, and understanding the role of terrestrial ecosystems in the global carbon balance, *Global Biogeochem. Cycles*, *12*, 25–34.
- Kim, C. P., and D. Entekhabi (1998), Feedbacks in the land-surface and mixed-layer energy budgets, *Boundary Layer Meteorol.*, *88*, 1–21.
- McCarthy, H. R., R. Oren, A. C. Finzi, and K. H. Johnsen (2006), Canopy leaf area constrains [CO<sub>2</sub>]-induced enhancement of productivity and partitioning among aboveground carbon pools., *Proc. Natl. Acad. Sci. U. S. A.*, *103*, 19,356–19,361.
- Novick, K. A., P. C. Stoy, G. G. Katul, D. Ellsworth, M. B. S. Siqueira, J.-Y. Juang, and R. Oren (2004), Carbon dioxide and water vapor exchange in a warm temperate grassland, *Oecologia*, *138*, 259–274.
- Oosting, H. J. (1942), An ecological analysis of the plant communities of Piedmont, North Carolina, *Am. Midland Nat.*, *28*, 1–126.
- Oren, R., B. Ewers, P. Todd, N. Phillips, and G. G. Katul (1998), Water balance delineates the soil layer in which moisture affects canopy conductance, *Ecol. Appl.*, *8*, 990–1002.
- Palmroth, S., C. A. Maier, H. R. McCarthy, A. C. Oishi, H.-S. Kim, K. H. Johnsen, G. G. Katul, and R. Oren (2005), Contrasting responses to drought of forest floor CO<sub>2</sub> efflux in a Loblolly pine plantation and a nearby Oak-Hickory forest, *Global Change Biol.*, *11*, 1–14.
- Pan, Z., E. Takle, M. Segal, and R. Turner (1996), Influences of model parameterization schemes on the response of rainfall to soil moisture in the central United States, *Mon. Weather Rev.*, *124*, 1786–1802.
- Richards, J. A. (1999), *Remote Sensing Digital Image Analysis*, Springer, New York.
- Schimel, D. S. (1995), Terrestrial ecosystems and the carbon cycle, *Global Change Biol.*, *1*, 77–91.
- Siqueira, M., G. G. Katal, and C.-T. Lai (2002), Quantifying net ecosystem exchange by multilevel ecophysiological and turbulent transport models, *Adv. Water Resour.*, *25*, 1357–1366.
- Stoy, P., G. G. Katul, M. B. S. Siqueira, J.-Y. Juang, H. R. McCarthy, H.-S. Kim, C. Oishi, and R. Oren (2005), Variability in net ecosystem exchange from hourly to inter-annual timescales at adjacent pine and hardwood forests: A wavelet analysis, *Tree Physiol.*, *25*, 887–902.
- Stull, R. B. (1976), The energetics of entrainment across a density interface, *J. Atmos. Sci.*, *33*, 1260–1267.
- Stull, R. B. (1988), *An Introduction to Boundary Layer Meteorology*, 666 pp., Springer, New York.
- Tans, P. P., and J. W. C. White (1998), In balance, with a little help from the plants, *Science*, *281*, 183–184.
- Tennekes, H. (1973), A model for the dynamics of the inversion above a convective boundary layer, *J. Atmos. Sci.*, *30*, 558–567.
- Trenberth, K. E., and C. J. Guillemont (1996), Physical processes involved in the 1988 drought and 1993 floods in North America, *J. Clim.*, *9*, 1288–1298.
- D. N. Wear, and J. G. Greis (Eds.) (2002), Southern forest resource assessment, *Gen. Tech. Rep. SRS-53*, 635 pp., For. Serv. South. Res. Stn., U.S. Dept. of Agric., Asheville, N. C.
- Wetzel, P. J. (1990), A simple parcel method for prediction of cumulus onset and area-averaged cloud amount over heterogeneous land surfaces, *J. Appl. Meteorol.*, *29*, 516–523.
- Zilitinkevich, S. S. (1972), On the determination of the height of the Ekman boundary layer, *Boundary Layer Meteorol.*, *3*, 141–145.

M. Detto, Dipartimento di Ingegneria Idraulica, Ambientale, Infrastruttura viarie e del Rilevamento, Piazza Leonardo da Vinci, 32, Politecnico di Milano, I-20133 Milan, Italy.

J.-Y. Juang, G. G. Katul, H.-S. Kim, A. C. Oishi, A. Porporato, M. S. Siqueira, and P. C. Stoy, Nicholas School of the Environment and Earth Sciences, Box 90328, Duke University, Durham, NC 27708-0328, USA. (jj19@duke.edu)